I&EC research
Industrial & Engineering Chemistry Research
pubs.acs.org/IECR
Article

Experimental and Computational Investigation of the Role of P in Moderating Ethane Dehydrogenation Performance over Ni-Based Catalysts

Jeonghyun Ko, Jessica A. Muhlenkamp, Yolanda Bonita, Nicole J. LiBretto, Jeffrey T. Miller, Jason C. Hicks,* and William F. Schneider*

Cite This: *Ind. Eng. Chem. Res.* 2020, 59, 12666−12676

ABSTRACT: We investigated the influence of P incorporation into a Ni catalyst on ethane dehydrogenation (EDH). Density functional theory calculations on model Ni(111) and $Ni_2P(001)$ surfaces reveal that surface P generally decreases adsorption energies of fragments relevant to EDH at surface Ni sites but that P itself participates in binding some of these intermediates. These nonlinear influences of P cause CH_3CH_2-H activation to occur with similar facility on metal and phosphide surfaces, while CH_2CH-H activation, an indicator of coking tendency, has much greater barriers on the phosphide. We prepared Ni and Ni−P catalysts on an SBA-15 support to test these predictions. A Ni−P catalyst with a 2:1 ratio ($Ni_2P(2)$/SBA-15), corresponding to the Ni_2P phase, showed >80% ethylene selectivity during EDH at 873 K, compared to <1% ethylene selectivity on Ni/SBA-15, and maintained this selectivity up to 4 h time-on-stream. Diffuse reflectance infrared Fourier transform spectroscopy observations following ethylene exposure and heating under an inert flow indicate the appearance of carbon deposits on Ni/SBA-15 compared to ethylene desorption from $Ni_2P(2)$/SBA-15, consistent with predicted adsorption energy trends. Thermogravimetric analysis of spent EDH catalysts indicates significantly less carbon deposition on $Ni_2P(2)$/SBA-15 relative to Ni/SBA-15. The results highlight the potential of metal phosphides as selective and robust alkane dehydrogenation catalysts.

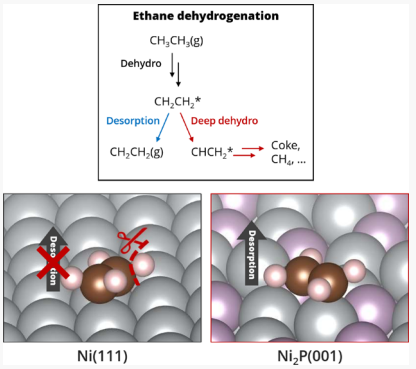

1. INTRODUCTION

Shale gas is emerging as an abundant source of light alkanes in the United States.[1] This abundance has created new opportunities in the petroleum and natural gas industry to produce transportation fuels and chemicals directly from shale gas.[2−7] Light hydrocarbons, like ethane, present a potentially tractable option for catalytic upgrading, and dehydrogenation to olefins is an attractive first step in that upgrading.[3,6] Steam cracking of ethane to ethylene requires high temperatures (1023−1223 K), is energy- and capital-intensive, and requires regular maintenance to remove coke from furnace tubes.[8−10] Catalytic ethane dehydrogenation (EDH) is an attractive, potentially less energy intensive, and more selective alternative to steam cracking:

$$C_2H_6 \rightarrow C_2H_4 + H_2 \quad (1)$$

EDH is endothermic ($\Delta H^{\circ}_{298\ K}$ = 137 kJ mol^{-1}), so temperatures approaching 1000 K are necessary to achieve useful conversions at atmospheric pressure.[3,11] At these temperatures, thermal cracking to undesired side products and deactivating coking compete with the desired ethylene product. The main challenges in catalytic dehydrogenation are thus (1) to increase ethylene selectivity and (2) to mitigate coke formation.

Pt catalysts are well known to be active for alkane dehydrogenation, but Pt suffers from poor selectivity and rapid catalyst deactivation arising from aggressive reaction with dehydrogenation intermediates.[12−16] Alloying of Pt with a second metal (including Sn,[12−14] Zn,[15] and In[16]) has been observed to suppress side reactions caused by this over-reactivity.[3] The increase in selectivity and stability over Pt-only catalysts is attributed to the creation of a smaller ensemble of Pt atoms on the surface and modifications of the electronic structure of surface Pt.[12−15,17−20] For example, Galvita et al.[13] observed an increase in ethylene selectivity and decrease in coke production with increasing Sn content (0−30%) in Pt-based, mixed Mg−Al oxide (Mg(Al)O)-supported catalysts based on EDH experiments performed at 873 K. Isotopic labeling experiments further identify ethylene itself as an intermediate in the production of methane and coke. Similarly,

Received: February 22, 2020
Revised: June 11, 2020
Accepted: June 16, 2020
Published: June 16, 2020

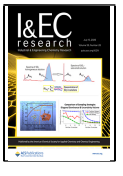

https://dx.doi.org/10.1021/acs.iecr.0c00908
Ind. Eng. Chem. Res. 2020, 59, 12666−12676

Cybulskis et al.[15] observed an increase in the EDH selectivity to ethylene at 873 K with the addition of Zn to Pt/SiO_2 catalysts. Density functional theory (DFT) calculations relate this improvement to a downshift of the Pt d-band and associated decrease in adsorbate-surface binding, in particular, of ethylene. Several DFT studies also reported that the d-band shift in Pt- and Pd-based alloy surfaces leads to weaker alkene-surface binding compared to that on pure Pd and Pt surfaces.[21−24] The energies of alkene desorption and alkene dehydrogenation (and/or C−C bond scission) as computed using DFT have been widely used to predict trends in alkene selectivity across metal alloy catalysts.[12,17,25−27] For example, Hook et al.[12,25] used supercell DFT models to compare C−H and C−C bond scission pathways over Pt(111) and $Pt_xSn/Pt(111)$ (x = 1, 3) model-ordered surfaces and found that absolute adsorption energies decrease and bond activation energies increase with increasing Sn content. These trends are attributed to a decrease in Pt ensemble size, which suppresses C−C bond scission pathways while maintaining C−H pathways, and modifications of the Pt electronic structure that facilitates ethylene desorption. This prediction is in agreement with the improved ethylene selectivity with increasing Sn content in Pt/Mg(Al)O catalysts from Galvita et al.'s experiments.[13,14]

Metal-rich phosphides are a potential alternative to Pt alloys as ethane dehydrogenation catalysts. In the high-metal-content regime, phosphides have metallic character, suggesting activities similar to bulk metals. Metal-rich phosphides can also present ensembles similar to those of metal alloys, potentially offering similar selectivity and coke resistance advantages, and tend to be strongly ordering, thus resisting loss of those ensembles at high temperatures.[26−28] Metal phosphide catalysts have outstanding hydrogenation activity[29−31] and have been explored for hydroprocessing, including hydrodesulfurization (HDS), hydrodenitrogenation (HDN), and hydrodeoxygenation (HDO).[26,32−36] Ni_2P is known to be the most active and selective phosphide-based hydroprocessing catalyst.[37−40] This hydrogenation performance has stimulated some interest in exploring the performance of Ni_2P for the reverse alkane dehydrogenation reaction.[41−44] Wang et al.[41] reported that Ni_2P relative to Ni supported on activated carbon (AC) had increased isobutane dehydrogenation conversion and selectivity to isobutene. The authors speculate that the charge transfer from Ni to P weakens Ni−C bonding and improves selectivity. Yao et al.[42] similarly reported that a $Ni_2P/\gamma\text{-}Al_2O_3$ catalyst is both more selective to propylene and produces less coke than a $Pt/\gamma\text{-}Al_2O_3$ catalyst when used for propane dehydrogenation at 893 K. Zhu et al.[43] found that a maximum in selectivity to isobutene occurred at a Ni/P ratio of 1, and they associated the high selectivity with the formation of a Ni_2P phase, as identified by X-ray diffraction (XRD). The authors found that when insufficient P was added during synthesis, phases other than Ni_2P formed, while addition of P above this ratio increased the acidity, resulting in reduced selectivity. They further found using Fourier transform infrared spectroscopy (FTIR) analysis that the $(CH_3)_2C{=}CH_2$ stretching band exhibits a larger red-shift when adsorbed on a Ni/SiO_2 catalyst than on a Ni_2P/SiO_2 one, consistent with weaker olefin adsorption on the latter and better resistance to coking.[43]

Herein, we expand upon the existing literature by using DFT calculations and spectroscopic and reaction measurements to interrogate the effects of P incorporation on the activity, selectivity, and durability of Ni-based catalysts toward EDH. We use DFT to compare analogous steps in ethane activation, ethylene production, and deactivation, focusing on Ni(111) and $Ni_2P(001)$ surfaces that share the same threefold Ni ensembles. We find that P both weakens the binding of carbon-containing species to the surface and, when isolating Ni ensembles, limits reactions, leading to deactivation, as has been proposed in the literature.[41,43] For experimental validation, we prepare, characterize, and evaluate Ni and a series of Ni−P materials with Ni/P ratios between 1 and 3 supported on SBA-15. We observe that P has beneficial impacts similar to those reported for metal alloys. Selectivity to ethylene is higher on the Ni−P/SBA-15 materials than on Ni/SBA-15. The 2:1 ratio material having the highest ethylene selectivity, denoted $Ni_2P(2)/SBA\text{-}15$. This improved selectivity is consistent with the greater resistance of $Ni_2P(2)/SBA\text{-}15$ than Ni/SBA-15 to coking when exposed to ethylene. The results highlight the underlying origins of the performance advantages induced by alloying a metal with phosphorus, in particular, the importance of surface electronic and ensemble effects in controlling metal phosphide reactivity.

2. METHODS

2.1. DFT Calculations. Density functional theory (DFT) calculations were performed with the Vienna Ab Initio Simulation Package (VASP).[45−47] Exchange-correlation energies were treated within the generalized gradient approximation (GGA)[48] using the Perdew−Burke−Ernzerhof (PBE) functional. Bulk lattice parameters were computed at a plane-wave cutoff of 520 eV and slab calculations with a wave cutoff of 400 eV. Ni calculations were performed spin-polarized; in test calculations, we found Ni_2P to have a negligible magnetic moment.

Bulk Ni is face-centered cubic, and the GGA-optimized lattice constant matches the experimental value of a = 3.52 Å.[49] Bulk Ni_2P is hexagonal (space group $P\bar{6}2m$) and consists of alternating Ni_3P_2 and Ni_3P planes stacked along the [001] direction. GGA-computed lattice parameters of $a = b$ = 5.88 Å and c = 3.37 Å are close to the experimental values of $a = b$ = 5.86 Å and c = 3.37 Å.[50] The Ni(111) and $Ni_2P(001)$ surfaces were modeled with five- and six-layer slabs, respectively, with a vacuum spacing of 15 Å. The bottom three layers were fixed at their bulk positions, and the remaining layers and adsorbates fully relaxed. The (3×3) and (1×1) surface unit cells were employed for Ni(111) and $Ni_2P(001)$. Supercell structures of Ni(111) and $Ni_2P(001)$ are shown in Figures S1 and S2, respectively. Monkhorst-Pack grids[51] of $3 \times 3 \times 1$ and $7 \times 7 \times 1$ k-points were selected for Ni(111) and $Ni_2P(001)$ from k-point convergence test calculations (Figure S3).

Geometries were relaxed to minima using the conjugate gradient algorithm until forces on unconstrained atoms were less than 0.02 eV/Å. The climbing image-nudged elastic band (CI-NEB) method was employed to determine the minimum energy paths and calculate the activation energies for surface reactions.[52] The vibrational spectra were obtained by calculating the Hessian matrix with finite differences of 0.015 Å. Each transition state was verified to have a single imaginary frequency along the reaction coordinate. Frequency calculation results are summarized in Tables S2 and S3. All atomic positions after geometry optimizations as well as full images of CI-NEB calculations with corresponding energy profiles are provided in the Supporting Information.

https://dx.doi.org/10.1021/acs.iecr.0c00908
Ind. Eng. Chem. Res. 2020, 59, 12666−12676

2.2. Catalyst Preparation. SBA-15 was used as the high-surface-area support and was synthesized using literature methods.[53,54] First, 18 g of a triblock copolymer (P-123, Aldrich) was dissolved overnight in an aqueous HCl solution consisting of 560 g of deionized (DI) H_2O and 100 g of HCl (Merck, 37% Fuming). Approximately 40 g of tetraethyl orthosilicate (Acros Organics, 98%) was added, and the solution was stirred at 308 K for 20 h followed by thermal treatment at 353 K for 24 h to swell the pores. The resulting product was filtered, washed with DI water until the filtrate was pH-neutral (approximately 750 mL), dried at least 12 h at 333 K, and calcined at 823 K for 6 h. Before use, the SBA-15 was vacuum-dried for 3 h at 473 K and stored in a N_2 glove box.

Ni−P/SBA-15 samples were prepared by first making an aqueous solution of citric acid (Alfa Aesar, 99%), $Ni(NO_3)_2 \cdot 6H_2O$ (Alfa Aesar, 99%), and $(NH_3)_2HPO_4$ (Amresco, 98%) at a citric acid-to-Ni molar ratio of 2 and the desired ratio of Ni to P. The resulting solution was added to SBA-15 using incipient wetness impregnation. The material was dried at 393 K for approximately 24 h and then calcined at 823 K for 3 h. The material was reduced with flowing hydrogen (Airgas, >99.995%) at 973 K for 2 h, cooled to room temperature under H_2, and then passivated with 1% O_2 in He mixture (Airgas, >99.995%) for 1 h. The nominal Ni loading of the catalyst was 10 wt %, and the nominal Ni-to-P ratio was varied from 3 to 1. Ni/SBA-15 was synthesized using the same process excluding the $(NH_3)_2HPO_4$ in the precursor solution and was reduced at 873 K. Ni reduces at a lower temperature than do the Ni−P materials. Therefore, we chose to reduce the Ni materials at reduction temperatures similar to those experienced under EDH conditions.[41,55,56]

2.3. Catalyst Characterization. In situ XRD measurements were performed at the 11-ID-C beamline at the Advanced Photon Source (APS) at the Argonne National Laboratory using X-rays of λ = 0.1173 Å (105.715 keV). Diffraction data were acquired using a PerkinElmer large-area detector. The high-energy and high-flux X-rays are necessary for collecting diffraction patterns on nanoparticles less than 10 nm in size to increase the signal-to-noise ratio and reduce the background from the support. The high energy of the synchrotron XRD results in patterns at lower 2θ than laboratory-scale XRD (e.g., less than about 10°). Samples were pressed into a self-supported pellet and loaded into a thermal stage. The cell was initially purged with He to remove any air prior to introducing a stream of 3.5% H_2/He at 100 mL/min. The temperature was subsequently increased to 823 K for analysis. After the diffraction measurements were completed at the reduction temperature, the cell was cooled to 308 K and a second diffraction measurement was obtained. The background scattering of the empty cell and SBA-15 was obtained under the same conditions and subtracted from the XRD patterns. The collected Debye−Scherrer ring diffraction patterns were integrated using Fit2D software to obtain intensity vs 2θ diffraction patterns. Theoretical diffraction patterns for possible structures were simulated at room temperature using crystal information files imported to Materials Analysis Using Diffraction (MAUD)[57] and used to identify the catalyst phase.

In situ X-ray absorption spectroscopy (XAS) experiments were performed at the 10-BM beamline at the APS. Measurements were performed at the Ni K (8.333 keV) edge for each sample. Samples were pressed into a stainless-steel sample holder and placed in a quartz tube sample cell. The cell was sealed and treated at 823 K in 3.5% H_2, cooled to room temperature in He, and then transferred to the beamline. The measurements were performed in transmission mode in fast scan from 8132 to 9000 eV. The data were interpreted using WinXAS 3.1 software to find the coordination number (CN) and bond distance (R) using standard procedures.[58,59] FEFF6 software was used to simulate Ni−Ni (CN = 12, BD = 2.49 Å) and Ni−P (CN = 1, BD = 2.25 Å) scattering pairs.

High-resolution transmission electron microscopy (HR-TEM) images were collected using a Titan 80-300 microscope. Samples for TEM were suspended in acetone using sonication, then drop-casted onto a carbon-coated copper grid, and dried in a desiccator. Thermogravimetric analysis (TGA) of spent catalysts was done using a Mettler Toledo Star 1 unit. The method was performed at a 5 K/min ramp rate from room temperature to 523 K and held for 10 h to remove any physisorbed species, such as water, from the sample. Then, the sample was further ramped at 5 K/min to 1073 K all in dry air at 20 mL/min. The mass loss between 548 and 1048 K was attributed to carbon species on the catalyst and support.

2.4. Ethane Dehydrogenation Experiments. Ethane dehydrogenation experiments were conducted in a 5 mm ID quartz reactor. Catalysts used for reaction were pelletized and sieved to 150−250 μm after calcination and then reduced as described in Section 2.2. The catalyst mass was varied between 5 and 50 mg and diluted with silica gel (Davisil, 150−250 μm, Sigma Aldrich). The reaction conditions were 50% ethane (Airgas, 99.9%), balance H_2, and 873 K. The reactor effluent was analyzed using an Agilent 7820A gas chromatograph with a thermal conductivity detector. Before each reaction, the catalyst was pretreated at 873 K for 1 h under a flow of 30 mL/min H_2. $Ni_2P(2)$/SBA-15 and Ni/SBA-15 were compared at 3% conversion. This conversion was chosen to remain below the equilibrium conversion for dehydrogenation (which is approximately 5.7% to ethylene). Additionally, this conversion was selected such that the products were in sufficient concentrations to accurately quantify.

2.5. FTIR Experiments. Diffuse reflectance infrared Fourier transform spectroscopy (DRIFTS) was used to examine ethylene (Airgas, 99.9%) adsorption on the catalyst surface using a Bruker Vertex 70 with a Harrick praying mantis high-temperature cell with ZnSe windows. The spectra were collected at a 4 cm^{-1} resolution with a 6 mm aperture, and a liquid N_2-cooled mercury−cadmium−telluride (MCT) detector. KBr (~80 mg) was placed into the sample cup, followed by ~15 mg of sample on top of KBr. The sample was pressed into a relatively flat surface before it was pretreated with H_2 at 30 mL/min for 2 h at 588 K. After pretreatment, 45 mL/min He was introduced into the cell, and the background spectra were taken at 588, 423, and 298 K. Ethylene gas (12 mL/min) was then flowed into the cell at 298 K until the signal did not change in intensity. The cell was purged with 45 mL/min He, and the spectra were collected until the intensity was constant at the same temperatures where the background spectra were taken. For the controlled oxidation experiments, 1% O_2 in He stream was introduced to the cell at 588 K. The spectra were then taken after 30 and 130 min of exposure to 1% O_2 in He.

3. RESULTS AND DISCUSSION

3.1. DFT Comparison of Ni(111) and Ni_2P(001) Surface Chemistries. We first turn to DFT to highlight the potential influences of P incorporation into Ni on EDH reactivity using Ni_2P as a model phosphide. To minimize

https://dx.doi.org/10.1021/acs.iecr.0c00908
Ind. Eng. Chem. Res. 2020, 59, 12666−12676

effects arising from gross structural differences between the two model substrates, we focus on the close-packed Ni(111) surface termination and the geometrically similar Ni_3P_2 ("A") termination along the (001) direction of $Ni_2P(001)$ (Figure 1). Both models contain Ni_3 ensembles, contiguous on Ni and isolated by P atoms on $Ni_2P(001)$. The Ni_3P ("B") termination along the (001) direction presents similar ensembles (Figure S2), and both terminations are identified in scanning tunneling microscopy (STM) and photoemission electron spectroscopy (PEEM) observations of Ni_2P single crystals.[60,61] DFT calculations show that the A termination is lower in energy than B over a wide range of P chemical potentials.[62] Calculations on the A and B terminations lead to similar conclusions, and we focus the discussion here on the A results. Figures S4−S7 compare computational results on the two terminations.

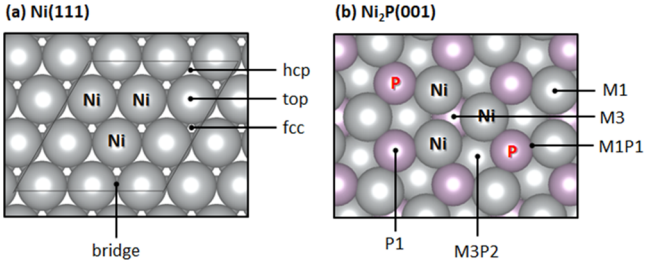

Figure 1. Top views of (a) the Ni(111) and (b) A-termination of $Ni_2P(001)$. Computational supercells are indicated with light lines, Ni atoms shown in gray, P shown in lavender, and adsorption sites labeled on each surface.

We compared the site preferences and binding energies of hydrogen and relevant C1 and C2 hydrocarbon species (C, CH, CH_2, CH_3, $CHCH_2$, CH_2CH_2, CH_2CH_3, and CH_3CH_3) on Ni(111) and $Ni_2P(001)$. We identified four unique adsorption sites on Ni(111) and five on $Ni_2P(001)$ (Figure 1), placed each adsorbate at each adsorption site, and relaxed the systems. Adsorption energies E_{ads} and site preferences are summarized in Table S1. To highlight the influence of P on adsorption characteristics, we compared the structures and energies of adsorbates constrained to the Ni_3 ensembles (Figure 2a) and at the lowest-energy sites on both surfaces. For this comparison, adsorbates at the Ni_3 ensembles were initialized in configurations corresponding with the lowest-energy configurations on Ni(111). Resultant optimized structures are summarized in Figures S9−S12. We define the relative adsorption energy $E_{rel} = E_{ads,Ni2P(001)} - E_{ads,Ni(111)}$ such that $E_{rel} > 0$ implies weaker binding on the $Ni_2P(001)$. Figure 2b shows DFT-computed E_{rel} of H, C1, and C2 hydrocarbon species constrained to Ni_3 ensemble sites (black bars) and in the lowest-energy configuration (red bars). Binding of C-containing species is diminished by up to 0.75 eV at the metal phosphide Ni_3 sites, despite similar adsorption geometries. As shown in Figure S13, the Ni d-electron densities of states (d-DOS) and d-band center (ε_d) are shifted to approximately 0.4 eV lower energy on $Ni_2P(001)$ relative to Ni(111), consistent

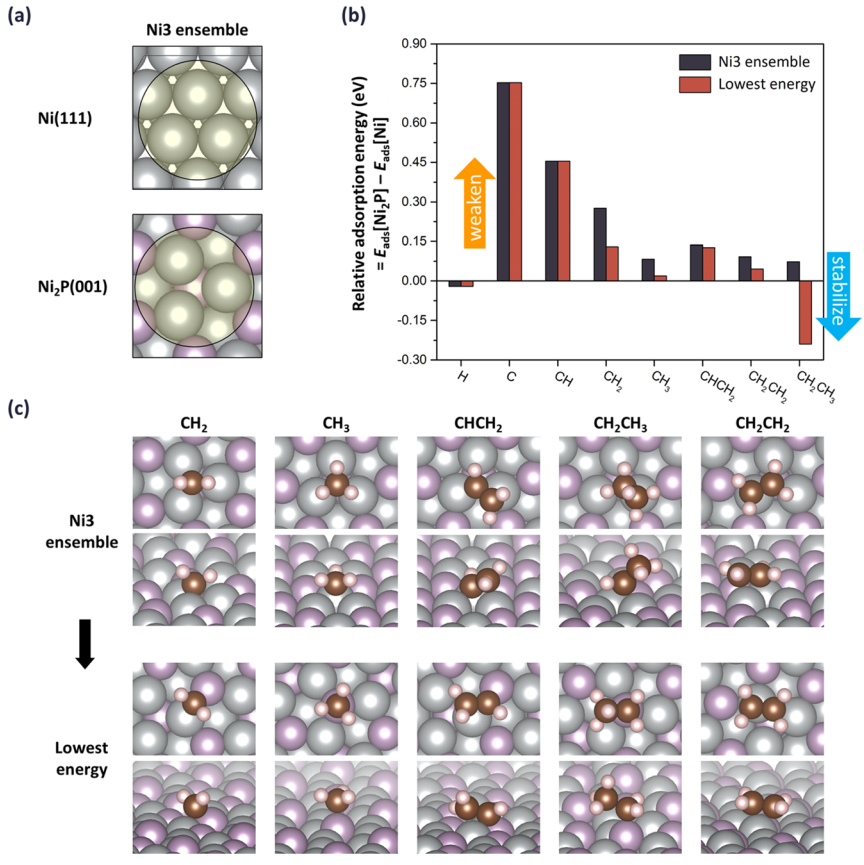

Figure 2. (a) Ni_3 ensembles on Ni(111) and $Ni_2P(001)$. (b) Adsorption energies on $Ni_2P(001)$ relative to Ni(111). Black and red bars correspond to adsorption confined to the Ni_3 ensemble and to lowest-energy sites, respectively. (c) Binding configurations of sp^2 and sp^3 hydrocarbons at the Ni_3 ensemble (first and second rows) and their lowest-energy sites (third and fourth rows).

https://dx.doi.org/10.1021/acs.iecr.0c00908
Ind. Eng. Chem. Res. 2020, 59, 12666−12676

with a general decrease in adsorbate binding.[63,64] DFT calculations similarly show that alloying of Pt with Sn results in a decrease in adsorbate binding from Pt(111) to $Pt_3Sn(111)$.[12,17,22,65−67]

While H, C, and CH prefer to adsorb on the Ni_3 ensemble sites (Figure S9), sp^2 CH_2 and $CHCH_2$ preferentially adsorb at Ni−P bridge sites, and sp^3 CH_3 and CH_2CH_3 prefer to adsorb atop P (Figure 2c). The energy difference is greatest for CH_2CH_3, which goes from a positive to negative E_{rel} when P sites are considered. This participation of P itself in the surface chemistry stands in contrast to $Pt_3Sn(111)$,[12,17,22,65−67] where similar calculations show that all species relevant to dehydrogenation prefer Pt_3 ensemble sites.

3.2. Comparison of Initial Ethane Dehydrogenation on Ni with Ni_2P. To compare relative activities toward ethane C−H bond activation, we computed reaction pathways for the initial ethane C−H activation ($CH_3CH_3(g) + * \rightarrow CH_2CH_3* + H*$) on Ni(111) and $Ni_2P(001)$. Within the DFT model here, ethane weakly physisorbs with no site specificity on both surfaces. As reported in Figure 3, we computed reaction pathways from arbitrary initial states to the lowest-energy product configuration, including ethyl and H adsorbed at second nearest-neighbor fcc sites on Ni(111) and ethyl at a P1 site and H at the neighboring M3 site on $Ni_2P(001)$. Both pathways exhibit two transition states, corresponding to C−H bond breaking (TS1) and diffusion of intermediate species (TS2). C−H bond breaking (TS1) occurs across Ni sites on both surfaces with similar activation energies (TS1 in Figure 3). After C−H bond breaking, intermediates diffuse away from each other to minimize adsorbate−adsorbate repulsive interactions and to adopt preferred binding sites. In this step on Ni(111), ethyl diffuses from the top site to the fcc hollow site with a negligible energy barrier (0.03 eV). On $Ni_2P(001)$, adsorbed ethyl and H diffuse simultaneously (TS2 in Figure 3) to their preferred P1 and M3 sites, respectively, with a barrier of 0.16 eV. The only notable difference between the two surfaces is the substantially greater lateral repulsion energy on $Ni_2P(001)$ than on Ni(111).

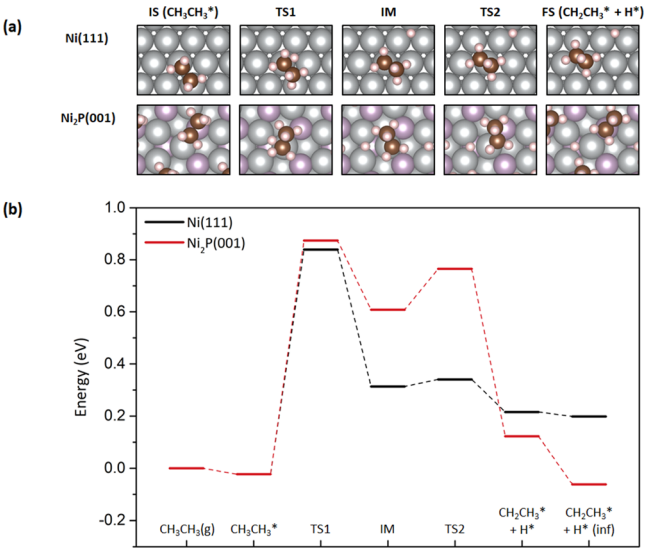

Figure 3. (a) Geometric structures of initial state (IS), intermediate state (IM), transition states (TS1 and TS2), and final state (FS) for ethane dehydrogenation on Ni(111) and $Ni_2P(001)$. (b) Energy profiles of ethane dehydrogenation to ethyl on Ni(111) and $Ni_2P(001)$. Black and red curves indicate the energy profiles on Ni(111) and $Ni_2P(001)$, respectively.

Thus, these computational results suggest that P incorporation will have at most a modest influence on C−H activation activity based on nearly identical C−H bond activation energies. As we describe more fully below, ethane is converted to hydrocarbon-based products over both Ni/SBA-15 and Ni−P/SBA-15, consistent with the activity predictions. Absolute activity comparisons are complicated by deactivation of the catalyst at reaction conditions.

3.3. Comparison of Ethylene Selectivity on Ni and Ni_2P. Selectivity is of paramount importance in EDH. We adopt a computational approach inspired by previous works[12,17,25,65,68] and use the difference between ethylene desorption ($CH_2CH_2* \rightarrow CH_2CH_2(g) + *$) and ethylene dehydrogenation ($CH_2CH_2* + * \rightarrow CHCH_2* + H*$) energies as a selectivity indicator. Again, we chose energy-minimizing initial and final states. As shown in Figure 2b, $CHCH_2*$ energies at the Ni_3 ensemble and the M1P1 sites are comparable. We compared H−$CHCH_2$ activations leading to either site on $Ni_2P(001)$; both pathways lead to similar conclusions and are compared in Figure S8.

As reported in Figure 2 and indicated in Figure 4b, ethylene adsorption/desorption energies are computed to be nearly identical on Ni(111) and $Ni_2P(001)$, as are H* and $CHCH_2*$ adsorption energies. The computed reaction pathways connecting these initial and final states are quite different, however. On Ni(111), C−H bond cleavage takes place from the initial fcc-top site and the elongated H atom binds onto a neighboring top site (TS in Figure 4). In contrast, when starting from the lowest-energy CH_2CH_2 site on $Ni_2P(001)$, ethylene must rotate and move to an M1P1 site to activate its C−H bond and the elongated H is located at the nearest Ni atom. As a result, the activation energies for ethylene

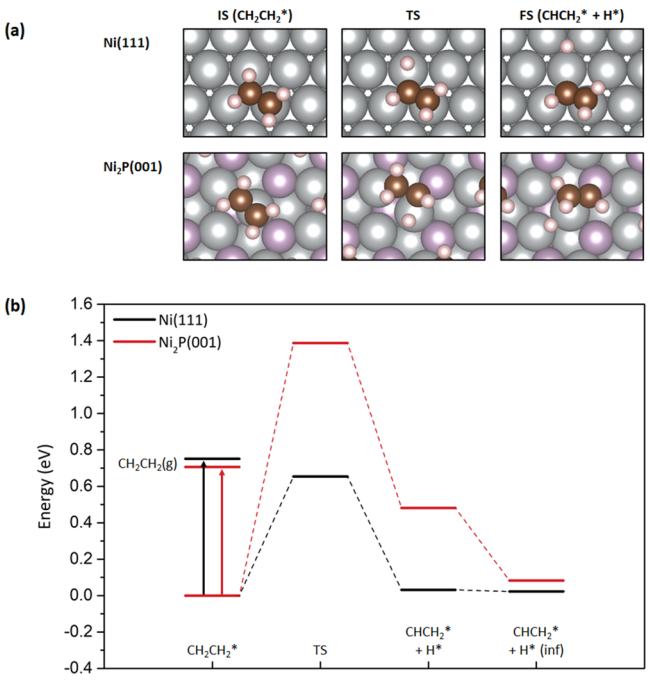

Figure 4. (a) Initial state (IS), transition state (TS), and final state (FS) structures for ethylene dehydrogenation on Ni(111) and $Ni_2P(001)$. (b) Relative energies for dehydrogenation vs ethylene desorption on Ni(111) (black) and $Ni_2P(001)$ (red).

https://dx.doi.org/10.1021/acs.iecr.0c00908
Ind. Eng. Chem. Res. 2020, 59, 12666−12676

dehydrogenation are much greater on $Ni_2P(001)$ than on Ni(111). After C−H bond cleavage on Ni(111), vinyl remains at an fcc-top site, while dissociated H migrates to an hcp hollow site. On $Ni_2P(001)$, vinyl rotates again to reach its preferred adsorption configuration and H is located at an M2 site. Unlike Ni(111), the H atom is blocked from the preferred M3 site by the vinyl species. The isolation of the Ni_3 ensemble by P thus constrains the ethylene dehydrogenation pathway and increases the activation energy for this. The DFT results of Figure 4b thus suggest that P incorporation into Ni will improve ethylene selectivity. These results highlight the contrast between ensemble effects on Ni_2P and Pt_3Sn: on the latter,[12,17] $H-CH_2CH_3$ and $H-CHCH_2$ activations occur along similar pathways, while on Ni_2P, the two pathways diverge because of the strong preference of $CHCH_2$* to associate with P.

We measured ethylene selectivity during ethane dehydrogenation experiments on Ni/SBA-15 and Ni−P/SBA-15, varying the Ni/P ratio from approximately 3:1 to 1:1. SBA-15 was chosen as a support due to its large specific surface area, uniform pore size distribution, and high thermal stability.[54] We found that a Ni/P ratio of 2, denoted as $Ni_2P(2)$/SBA-15, showed the highest ethylene selectivity (Figure S14), as discussed in more detail below. Thus, we selected the $Ni_2P(2)$/SBA-15 sample for further analysis.

The phase of the $Ni_2P(2)$/SBA-15 material was analyzed using synchrotron XRD. The X-ray energy was 105.715 keV, resulting in diffraction patterns at a low 2θ angle, e.g., of less than 10°, compared with laboratory XRD. The high flux of synchrotron XRD gives a better signal-to-noise ratio, and the high-energy X-ray allows for increased sensitivity from Ni scattering. The resulting pattern is shown in Figure 5a and

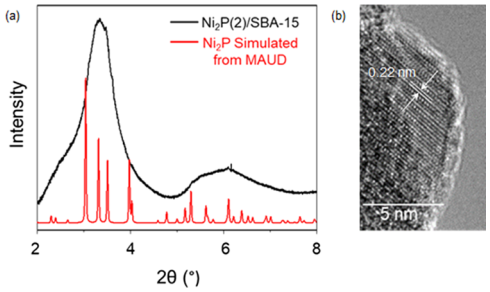

Figure 5. (a) Synchrotron XRD pattern and (b) HR-TEM image of $Ni_2P(2)$/SBA-15.

contains broad peaks in the regions, consistent with the Ni_2P phase.[69] Due to the broad nature of the peaks, the phase purity of this material is inconclusive. HR-TEM analysis was also performed, and d-spacing of 0.22 nm was observed, which was consistent with the (111) plane of Ni_2P (Figure 5b).[69] The local structure of the Ni/SBA-15 and $Ni_2P(2)$/SBA-15 materials was probed with XANES and EXAFS analysis, and the results are provided in Table 1. The XANES energy (8.333 keV) is consistent with metallic Ni for both samples and subtle changes in the white line for $Ni_2P(2)$/SBA-15 are consistent with the addition of P. In Ni/SBA-15, there are 6.8 Ni−Ni bonds at 2.47 Å, whereas the addition of P leads to the elongation of Ni−Ni bonds in $Ni_2P(2)$/SBA-15. In $Ni_2P(2)$/SBA-15, there are 2.0 Ni−Ni bonds at 2.54 Å and 2.7 Ni−P bonds at 2.25 Å, consistent with the ideal Ni_2P phase. The coordination number ratio (CN_{Ni-P}/CN_{Ni-Ni}) is approximately 1.5, which is consistent with a Ni_2P structure. The difference in the optimum Ni/P ratio seen here relative to the optimum Ni/P ratio reported for isobutane dehydrogenation by Zhu et al.[43] could be due to differences in the catalyst preparation and pretreatment conditions. Here, we report experimentally determined compositions from elemental analysis (Table S6), whereas the previous literature used nominal values. Because P is commonly lost during the TPR synthesis method, the optimum composition aligns with the Ni_2P phase.[43,70] Additional characterization of these materials including surface area, bulk composition, and particle size analysis is given in Table S6 and Figure S15.

As mentioned earlier, both Ni and Ni_2P catalysts activate ethane but have different product distributions. Figure 6a shows ethylene selectivity for Ni/SBA-15 and $Ni_2P(2)$/SBA-15 during a 4 h time-on-stream EDH experiment. The catalyst mass and total flow rate were varied such that both $Ni_2P(2)$/SBA-15 and Ni/SBA-15 had similar conversion profiles with conversions of approximately 3% after the initial deactivation period (roughly the first hour) (Figure S16). The ethylene selectivity over Ni/SBA-15 was <1%, while the ethylene selectivity over $Ni_2P(2)$/SBA-15 was >80%. The ethylene selectivity of $Ni_2P(2)$/SBA-15 decreased with increasing conversion. However, it remained well above the ethylene selectivity of Ni/SBA-15 throughout the conversion range evaluated (up to 8% conversion). Ethylene selectivity varied with the Ni/P ratio (Figure S14). This dependence could be due to variations in the structure with composition, which have been shown to affect isobutane dehydrogenation performance of Ni−P catalysts.[43] Even with this variation, all Ni/P ratios showed higher ethylene selectivity than Ni/SBA-15. This improved ethylene selectivity for Ni−P/SBA-15 materials over Ni/SBA-15 matches the trends reported in the literature for isobutane and propane dehydrogenation with similar materials.[41−43] These results also corroborate the computationally predicted selectivity trend. Figure 6b shows the apparent ethylene production rate for both $Ni_2P(2)$/SBA-15 and Ni/SBA-15. Both materials show the expected decrease in activity

Table 1. XANES Energy and Fitted Bond Distances from EXAFS for $Ni_2P(2)$/SBA-15 and Ni/SBA-15[a]

sample	XANES energy (keV)	scattering pair	CN	R (Å)	σ^2 (Å^2)	ΔE_o (eV)
Ni_2P (ideal structure)	structural simulation (Ni bound to 4 P)	Ni−P	4	2.24 (avg)		
		Ni−Ni	2	2.65 (avg)		
	structural simulation (Ni in center)	Ni−P	3	2.24 (avg)		
		Ni−Ni	3	2.64 (avg)		
Ni/SBA-15	8.333	Ni−Ni	6.8	2.47	0.005	4.1
$Ni_2P(2)$/SBA-15	8.333	Ni−P	2.7	2.25	0.005	5.8
		Ni−Ni	2.0	2.54	0.005	

[a]CN is the coordination number. R is the bond distance. σ^2 and E_o are EXAFS fitting parameters.

https://dx.doi.org/10.1021/acs.iecr.0c00908
Ind. Eng. Chem. Res. 2020, 59, 12666−12676

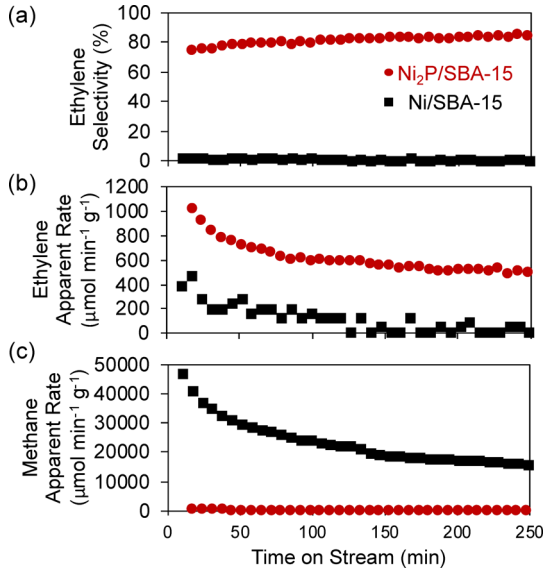

Figure 6. (a) Ethylene selectivity, (b) ethylene production rate, and (c) methane production rate for $Ni_2P(2)$/SBA-15 (red circles) and Ni/SBA-15 (black squares) during ethane dehydrogenation. Both materials were run at approximately 3% conversion.

with time due to deactivation. At the start of the reaction, $Ni_2P(2)$/SBA-15 produces ethylene over twice the rate as Ni/SBA-15. After 4 h, the ethylene production rate with $Ni_2P(2)$/SBA-15 is over 10 times the rate of Ni/SBA-15. Figure 6c shows the methane production rate over both materials. Ni/SBA-15 makes significant quantities of methane, while $Ni_2P(2)$/SBA-15 produces negligible quantities of methane. $Ni_2P(2)$/SBA-15 is, therefore, a superior EDH catalyst compared to Ni/SBA-15.

The differences in methane productivity could be indicative of differences in the activity for C−C bond breaking. To test this idea, we computed activation barriers for C−C bond cleavage on the Ni and Ni_2P models. Activation barriers on the two models are similar: 2.31 and 2.52 eV for ethane dissociation ($CH_3CH_3^* + * \rightarrow CH_3^* + CH_3^*$) on Ni(111) and $Ni_2P(001)$, respectively, and 1.19 and 1.12 eV for ethylene dissociation ($CH_2CH_2^* + * \rightarrow CH_2^* + CH_2^*$) on Ni(111) and $Ni_2P(001)$, respectively (Tables S4 and S5). From comparisons with Figure 3, CH_3CH_2-H activation is more likely on either catalyst than is CH_3-CH_3 activation; similarly, from comparisons with Figure 4, ethylene desorption is much more likely on either catalyst than is $CH_2{=}CH_2$ activation, supporting our choice of the quantities in Figures 3 and 4 to differentiate the performance of the two materials. Methane likely arises from C−C cleavage reactions of more deeply dehydrogenated intermediates, as has been proposed on other metals.[12,71] In fact, the greater affinity of Ni than Ni_2P for C* and CH* (Figure 2b) is consistent with a greater activity for both carbon and methane (through hydrogenation of deeply hydrogenated intermediates) production on Ni than Ni_2P.

Galvita et al.[13] proposed that ethylene readsorption and subsequent reaction contributes to catalyst deactivation on Pt/Mg(Al)O and that Sn addition promotes ethylene desorption. Here, calculations suggest that P plays a similar role to that of Sn such that ethylene desorbs more readily from Ni_2P than from Ni (Figure 4b). To test these differences, we compared the products of ethylene adsorption and reaction on Ni vs Ni_2P using DRIFTS to interrogate surface intermediates.

Ethylene was adsorbed on either Ni/SBA-15 or $Ni_2P(2)$/SBA-15 followed by a He purge at various temperatures (298, 423, and 588 K; Figure 7). The spectra of both Ni/SBA-15 and

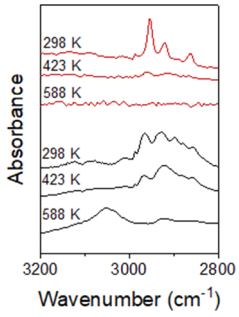

Figure 7. DRIFTS experiments after room-temperature ethylene exposure and subsequent heating on $Ni_2P(2)$/SBA-15 (red) and Ni/SBA-15 (black).

$Ni_2P(2)$/SBA-15 at 298 K show C−H stretches in the 2800−3000 cm^{-1} region from ethylene and ethylene-derived hydrocarbons. The resulting spectrum from the Ni/SBA-15 sample is similar to literature reports for ethylene adsorbed at room temperature on Ni/SiO_2.[72,73] For Ni/SBA-15, the features in this region are broader than for $Ni_2P(2)$/SBA-15, indicating that a variety of hydrocarbon species are present on Ni/SBA-15 relative to $Ni_2P(2)$/SBA-15 upon ethylene adsorption. At higher temperatures (423 and 588 K) for $Ni_2P(2)$/SBA-15, the C−H stretching features are absent, indicating that the hydrocarbons have desorbed from the surface and corroborates the computational predictions. For Ni/SBA-15 at 423 K, the C−H features in the 2800−3000 cm^{-1} region remain. At 588 K on Ni/SBA-15, residual C−H stretches are present at ∼2925 cm^{-1} as well as the formation of a new, broad feature centered at ∼3055 cm^{-1}. Both olefinic and aromatic C−H stretches appear at >3000 cm^{-1}.[74,75] However, the olefinic feature of ethylene in this region is usually only visible at sub-ambient temperatures.[76,77] Therefore, this feature is likely related to aromatic C−H stretches from carbon growth on the catalyst and indicates that further dehydrogenation into these aromatic species is more prevalent on Ni/SBA-15 than $Ni_2P(2)$/SBA-15, consistent with computational predictions.

3.4. Comparison of Coke Formation on Ni and Ni_2P.

Coking occurs by surface decomposition of hydrocarbons and aggregation of carbon-containing adsorbates to form carbonaceous species.[78] The adsorption energy of atomic C has been proposed to be a descriptor of coking tendency,[79,80] and from Figure 2b, the binding energies of both C* and CH* are diminished with the incorporation of P into Ni.

To contrast the coking tendency of Ni and Ni_2P, we return to the ethylene DRIFTS experiments. In the 588 K spectrum for Ni/SBA-15, we attributed the feature at 3055 cm^{-1} to aromatic carbon deposits on the surface.[74−77] To further probe this assignment, we performed an in situ-controlled oxidation by exposing the Ni/SBA-15 sample after ethylene adsorption and heating to 588 K to a 1% O_2 stream. Figure S17 shows the spectrum of Ni/SBA-15 before and after controlled oxidation for 30 and 130 min. With increasing exposure to 1% O_2 in He, the feature at 3055 cm^{-1} diminishes, likely due to oxidation of the remaining surface hydrocarbon species. The feature at 3055 cm^{-1} is not present in the 588 K spectrum for $Ni_2P(2)$/SBA-15 shown in Figure 7. Instead, the hydrocarbons on the

https://dx.doi.org/10.1021/acs.iecr.0c00908
Ind. Eng. Chem. Res. 2020, 59, 12666−12676

$Ni_2P(2)$/SBA-15 surface are able to desorb from the surface. This is further corroborated by TGA analysis of the spent catalysts after EDH. $Ni_2P(2)$/SBA-15 showed over three times less carbon formation (96 mg C/g catalyst) over the course of the EDH reaction than Ni/SBA-15 (360 mg C/g catalyst). This is consistent with the lack of evidence of carbon deposits in the high-temperature $Ni_2P(2)$/SBA-15 ethylene IR spectra and the computationally predicted carbon deposition resistance for $Ni_2P(2)$/SBA-15 relative to Ni/SBA-15.

4. CONCLUSIONS

We have compared Ni and Ni_2P to probe the effects of P incorporation on EDH performance via computational and experimental techniques. We find that smaller and isolated Ni ensembles surrounded by P atoms, present on the $Ni_2P(001)$ facet, have distinct geometric and electronic features that promote EDH performance relative to Ni(111). The small size of the Ni_3 ensembles causes some reaction steps to involve surface P atoms, with the consequence for the relative ability to activate sp^3 and sp^2 C−H bonds. Further, the binding energies of C atoms, likely precursors to coke, are diminished on Ni_2P relative to Ni, an effect that can be traced back to shifts in the d-band of surface Ni atoms. While we expect quantitative differences on different facets of Ni_2P, we expect these distinguishing features of P incorporation to transfer across surfaces. Computational results do transfer across two different Ni_2P terminations, and computational inferences do align with experimental observation, lending support to these inferences.

For conventional Pt−Sn catalysts, a trade-off between intrinsic catalytic activity and alkene selectivity should be considered because of the increase in activation energies of the first dehydrogenation of alkane as well as the alkene dehydrogenation.[12,17] In contrast, intrinsic catalytic activity is likely to be maintained with enhanced alkene selectivity on Ni_2P because P atoms are selectively engaged in C−H bond breaking. Interestingly, this feature of Ni_2P seems to vary with different reactions and adsorbates. For example, a recent theoretical study of C−O bond rupture in 2-methyltetrahydrofuran (MTHF) reported that cleavage of the C−O bond of reaction intermediates always occurs at Ni ensembles over $Ni_2P(001)$ and $Ni_{12}P_5(001)$ and not at P sites.[81]

Last, we note that some opportunities remain to be explored for further improvements of metal phosphide catalysts given that the 80% ethylene selectivity of $Ni_2P(2)$/SBA-15 is still lower than Pt-based alloy catalysts (>90%) at similar experimental conditions.[13,16] One possible way to improve catalytic performance of Ni_2P catalyst is the use of an alkali promoter to reduce the acidity of catalyst. It was reported that a Cs promoter could increase selectivity to isobutene from 85 to 93% in isobutane dehydrogenation over the Ni_2P catalyst.[41] Another possibility is an exploration of different kinds of metal phosphides. Including this work, only Ni−P catalysts have been studied in alkane dehydrogenation,[41−44] even though other kinds of monometallic and bimetallic phosphides have been identified as excellent catalysts in different fields.[30,33,35,36,40] Thus, it is needed to explore various types of metal phosphide catalysts and to compare those results with this work for further improvement in metal phosphide EDH catalysts.

■ ASSOCIATED CONTENT

Supporting Information

The Supporting Information is available free of charge at https://pubs.acs.org/doi/10.1021/acs.iecr.0c00908.

DFT calculations, structures of slab models, k-point convergence tests, adsorption geometries of all adsorbates at the lowest-energy sites and Ni_3 ensemble sites on Ni(111) and Ni_2P-A(001), the d-electron density of states of surface metals on Ni(111) and Ni_2P-A(001), two possible ethylene dehydrogenation pathways on Ni_2P-A(001) and Ni_2P-B(001), adsorptions of all adsorbates and C−H bond cleavages of ethane and ethylene on Ni_2P-B(001), C−H and C−C bond cleavages of ethane and ethylene on Ni(111) and Ni_2P-A(001), vibration frequencies of transition states, summary of adsorption energies and site preferences on Ni(111) and Ni_2P-A(001), experiments, physical properties and TEM images of the samples, ethylene selectivity for different Ni/P ratios, ethane conversions as a function of time for $Ni_2P(2)$/SBA-15 and Ni/SBA-15, and the spectrum of Ni/SBA-15 before and after controlled oxidation (PDF)

Full set of CONTCARs for all the structures discussed in the paper (ZIP)

■ AUTHOR INFORMATION

Corresponding Authors

Jason C. Hicks − *Department of Chemical and Biomolecular Engineering, University of Notre Dame, Notre Dame, Indiana 46556, United States;* orcid.org/0000-0002-5054-2874; Email: jhicks3@nd.edu

William F. Schneider − *Department of Chemical and Biomolecular Engineering, University of Notre Dame, Notre Dame, Indiana 46556, United States;* orcid.org/0000-0003-0664-2138; Email: wschneider@nd.edu

Authors

Jeonghyun Ko − *Department of Chemical and Biomolecular Engineering, University of Notre Dame, Notre Dame, Indiana 46556, United States*

Jessica A. Muhlenkamp − *Department of Chemical and Biomolecular Engineering, University of Notre Dame, Notre Dame, Indiana 46556, United States*

Yolanda Bonita − *Department of Chemical and Biomolecular Engineering, University of Notre Dame, Notre Dame, Indiana 46556, United States*

Nicole J. LiBretto − *School of Chemical Engineering, Purdue University, West Lafayette, Indiana 47907, United States*

Jeffrey T. Miller − *School of Chemical Engineering, Purdue University, West Lafayette, Indiana 47907, United States;* orcid.org/0000-0002-6269-0620

Complete contact information is available at: https://pubs.acs.org/10.1021/acs.iecr.0c00908

Notes

The authors declare no competing financial interest.

■ ACKNOWLEDGMENTS

This work was supported in part by the Engineering Research Centers Program of the National Science Foundation under NSF Cooperative Agreement no. EEC-1647722. The computing resources and technical support for this work were

provided by the Notre Dame Center for Research Computing. Y.B. and J.C.H. also thank the National Science Foundation through the CAREER award program (CBET-1351609), the Defense University Research Instrumentation Program under AFOSR Award no. FA9550-17-1-0376, and the Center of Environmental Science and Technology (CEST) for partial support of this work. J.A.M. and J.C.H. also thank CEST, Notre Dame Integrated Imaging Facility, and Notre Dame Materials Characterization Facility for the use of their facilities.

REFERENCES

(1) Bruijnincx, P. C. A.; Weckhuysen, B. M. Shale Gas Revolution: An Opportunity for the Production of Biobased Chemicals? *Angew. Chem., Int. Ed.* **2013**, *52*, 11980−11987.
(2) Stangland, E. E. Shale Gas Implications for C_2-C_3 Olefin Production: Incumbent and Future Technology. *Annu. Rev. Chem. Biomol. Eng.* **2018**, *9*, 341−364.
(3) Sattler, J. J. H. B.; Ruiz-Martinez, J.; Santillan-Jimenez, E.; Weckhuysen, B. M. Catalytic Dehydrogenation of Light Alkanes on Metals and Metal Oxides. *Chem. Rev.* **2014**, *114*, 10613−10653.
(4) Wang, B.; Albarracín-Suazo, S.; Pagán-Torres, Y.; Nikolla, E. Advances in Methane Conversion Processes. *Catal. Today* **2017**, *285*, 147−158.
(5) Bravo-Suárez, J. J.; Kidder, M. K.; Schwartz, V. *Novel Materials for Catalysis and Fuels Processing*; ACS Symposium Series. American Chemical Society: January 11321, 2013, p 0, DOI: 10.1021/bk-2013-1132.
(6) National Academies of Sciences, Engineering, and Medicine *The Changing Landscape of Hydrocarbon Feedstocks for Chemical Production: Implications for Catalysis: Proceedings of a Workshop*; Alper, J., Ed.; National Academies Press: Washington, DC, 2016.
(7) Park, M. B.; Park, E. D.; Ahn, W.-S. Recent Progress in Direct Conversion of Methane to Methanol Over Copper-Exchanged Zeolites. *Front. Chem.* **2019**, *7*, 514.
(8) Bhasin, M. M.; McCain, J. H.; Vora, B. V.; Imai, T.; Pujadó, P. R. Dehydrogenation and Oxydehydrogenation of Paraffins to Olefins. *Appl. Catal., A* **2001**, *221*, 397−419.
(9) Porosoff, M. D.; Myint, M. N. Z.; Kattel, S.; Xie, Z.; Gomez, E.; Liu, P.; Chen, J. G. Identifying Different Types of Catalysts for CO2 Reduction by Ethane through Dry Reforming and Oxidative Dehydrogenation. *Angew. Chem., Int. Ed.* **2015**, *54*, 15501−15505.
(10) Avila, A. M.; Yu, Z.; Fazli, S.; Sawada, J. A.; Kuznicki, S. M. Hydrogen-Selective Natural Mordenite in a Membrane Reactor for Ethane Dehydrogenation. *Microporous Mesoporous Mater.* **2014**, *190*, 301−308.
(11) Myint, M.; Yan, B.; Wan, J.; Zhao, S.; Chen, J. G. Reforming and Oxidative Dehydrogenation of Ethane with CO2 as a Soft Oxidant over Bimetallic Catalysts. *J. Catal.* **2016**, *343*, 168−177.
(12) Hook, A.; Massa, J. D.; Celik, F. E. Effect of Tin Coverage on Selectivity for Ethane Dehydrogenation over Platinum−Tin Alloys. *J. Phys. Chem. C* **2016**, *120*, 27307−27318.
(13) Galvita, V.; Siddiqi, G.; Sun, P.; Bell, A. T. Ethane Dehydrogenation on Pt/Mg(Al)O and PtSn/Mg(Al)O Catalysts. *J. Catal.* **2010**, *271*, 209−219.
(14) Wu, J.; Peng, Z.; Bell, A. T. Effects of Composition and Metal Particle Size on Ethane Dehydrogenation over PtxSn100−x/Mg(Al)O (70⩽x⩽100). *J. Catal.* **2014**, *311*, 161−168.
(15) Cybulskis, V. J.; Bukowski, B. C.; Tseng, H.-T.; Gallagher, J. R.; Wu, Z.; Wegener, E.; Kropf, A. J.; Ravel, B.; Ribeiro, F. H.; Greeley, J.; et al. Zinc Promotion of Platinum for Catalytic Light Alkane Dehydrogenation: Insights into Geometric and Electronic Effects. *ACS Catal.* **2017**, *7*, 4173−4181.
(16) Wegener, E. C.; Wu, Z.; Tseng, H.-T.; Gallagher, J. R.; Ren, Y.; Diaz, R. E.; Ribeiro, F. H.; Miller, J. T. Structure and Reactivity of Pt−In Intermetallic Alloy Nanoparticles: Highly Selective Catalysts for Ethane Dehydrogenation. *Catal. Today* **2018**, *299*, 146−153.
(17) Yang, M.-L.; Zhu, Y.-A.; Zhou, X.-G.; Sui, Z.-J.; Chen, D. First-Principles Calculations of Propane Dehydrogenation over PtSn Catalysts. *ACS Catal.* **2012**, *2*, 1247−1258.
(18) Hill, J. M.; Shen, J.; Watwe, R. M.; Dumesic, J. A. Microcalorimetric, Infrared Spectroscopic, and DFT Studies of Ethylene Adsorption on Pd and Pd/Sn Catalysts. *Langmuir* **2000**, *16*, 2213−2219.
(19) Bariås, O. A.; Holmen, A.; Blekkan, E. A. Propane Dehydrogenation over Supported Pt and Pt−Sn Catalysts: Catalyst Preparation, Characterization, and Activity Measurements. *J. Catal.* **1996**, *158*, 1−12.
(20) Hill, J. M.; Cortright, R. D.; Dumesic, J. A. Silica- and L-Zeolite-Supported Pt, Pt/Sn and Pt/Sn/K Catalysts for Isobutane Dehydrogenation. *Appl. Catal., A* **1998**, *168*, 9−21.
(21) Cai, W.; Mu, R.; Zha, S.; Sun, G.; Chen, S.; Zhao, Z.-J.; Li, H.; Tian, H.; Tang, Y.; Tao, F. F.; Zeng, L.; Gong, J. Subsurface Catalysis-Mediated Selectivity of Dehydrogenation Reaction. *Sci. Adv.* **2018**, *4*, No. eaar5418.
(22) Nykänen, L.; Honkala, K. Density Functional Theory Study on Propane and Propene Adsorption on Pt(111) and PtSn Alloy Surfaces. *J. Phys. Chem. C* **2011**, *115*, 9578−9586.
(23) Zellner, M. B.; Goda, A. M.; Skoplyak, O.; Barteau, M. A.; Chen, J. G. Trends in the Adsorption and Decomposition of Hydrogen and Ethylene on Monolayer Metal Films: A Combined DFT and Experimental Study. *Surf. Sci.* **2005**, *583*, 281−296.
(24) Sheth, P. A.; Neurock, M.; Smith, C. M. First-Principles Analysis of the Effects of Alloying Pd with Ag for the Catalytic Hydrogenation of Acetylene−Ethylene Mixtures. *J. Phys. Chem. B* **2005**, *109*, 12449−12466.
(25) Sun, G.; Zhao, Z.-J.; Mu, R.; Zha, S.; Li, L.; Chen, S.; Zang, K.; Luo, J.; Li, Z.; Purdy, S. C.; et al. Breaking the Scaling Relationship via Thermally Stable Pt/Cu Single Atom Alloys for Catalytic Dehydrogenation. *Nat. Commun.* **2018**, *9*, 4454.
(26) Oyama, S. T.; Gott, T.; Zhao, H.; Lee, Y.-K. Transition Metal Phosphide Hydroprocessing Catalysts: A Review. *Catal. Today* **2009**, *143*, 94−107.
(27) Wang, Y.; Li, X.; Sun, Z.; Wang, A. Metal Phosphides as High-Performance Hydrotreating Catalysts. *J. Jpn Pet. Inst.* **2015**, *58*, 197−204.
(28) Albani, D.; Karajovic, K.; Tata, B.; Li, Q.; Mitchell, S.; López, N.; Pérez-Ramírez, J. Ensemble Design in Nickel Phosphide Catalysts for Alkyne Semi-Hydrogenation. *ChemCatChem* **2018**, *11*, 457−464.
(29) Bonita, Y.; Hicks, J. C. Periodic Trends from Metal Substitution in Bimetallic Mo-Based Phosphides for Hydrodeoxygenation and Hydrogenation Reactions. *J. Phys. Chem. C* **2018**, *122*, 13322−13332.
(30) Bonita, Y.; O'Connell, T. P.; Miller, H. E.; Hicks, J. C. Revealing the Hydrogenation Performance of RuMo Phosphide for Chemoselective Reduction of Functionalized Aromatic Hydrocarbons. *Ind. Eng. Chem. Res.* **2019**, *58*, 3650−3658.
(31) Bonita, Y.; Jain, V.; Geng, F.; O'Connell, T. P.; Wilson, W. N.; Rai, N.; Hicks, J. C. Direct Synthesis of Furfuryl Alcohol from Furfural: Catalytic Performance of Monometallic and Bimetallic Mo and Ru Phosphides. *Catal. Sci. Technol.* **2019**, *9*, 3656−3668.
(32) Prins, R.; Bussell, M. E. Metal Phosphides: Preparation, Characterization and Catalytic Reactivity. *Catal. Lett.* **2012**, *142*, 1413−1436.
(33) Pei, Y.; Cheng, Y.; Chen, J.; Smith, W.; Dong, P.; Ajayan, P. M.; Ye, M.; Shen, J. Recent Developments of Transition Metal Phosphides as Catalysts in the Energy Conversion Field. *J. Mater. Chem. A* **2018**, *6*, 23220−23243.
(34) Bonita, Y.; Hicks, J. C. Chapter 3 Metal Phosphides and Their Applications in Catalysis. In *Alternative Catalytic Materials: Carbides, Nitrides, Phosphides and Amorphous Boron Alloys*; The Royal Society of Chemistry: 2018; pp 46−70.
(35) Rensel, D. J.; Rouvimov, S.; Gin, M. E.; Hicks, J. C. Highly Selective Bimetallic FeMoP Catalyst for C−O Bond Cleavage of Aryl Ethers. *J. Catal.* **2013**, *305*, 256−263.

https://dx.doi.org/10.1021/acs.iecr.0c00908
Ind. Eng. Chem. Res. 2020, 59, 12666−12676

(36) Rensel, D. J.; Kim, J.; Jain, V.; Bonita, Y.; Rai, N.; Hicks, J. C. Composition-Directed FeXMo2-XP Bimetallic Catalysts for Hydrodeoxygenation Reactions. *Catal. Sci. Technol.* **2017**, *7*, 1857−1867.
(37) Clark, P.; Wang, X.; Oyama, S. T. Characterization of Silica-Supported Molybdenum and Tungsten Phosphide Hydroprocessing Catalysts by 31P Nuclear Magnetic Resonance Spectroscopy. *J. Catal.* **2002**, *207*, 256−265.
(38) Wang, X.; Clark, P.; Oyama, S. T. Synthesis, Characterization, and Hydrotreating Activity of Several Iron Group Transition Metal Phosphides. *J. Catal.* **2002**, *208*, 321−331.
(39) Oyama, S. T. Novel Catalysts for Advanced Hydroprocessing: Transition Metal Phosphides. *J. Catal.* **2003**, *216*, 343−352.
(40) Cho, A.; Shin, J.; Takagaki, A.; Kikuchi, R.; Oyama, S. T. Ligand and Ensemble Effects in Bimetallic NiFe Phosphide Catalysts for the Hydrodeoxygenation of 2-Methyltetrahydrofuran. *Top. Catal.* **2012**, *55*, 969−980.
(41) Xu, Y.; Sang, H.; Wang, K.; Wang, X. Catalytic Dehydrogenation of Isobutane in the Presence of Hydrogen over Cs-Modified Ni_2P Supported on Active Carbon. *Appl. Surf. Sci.* **2014**, *316*, 163−170.
(42) Yao, Y.; Zuo, M.; Zhou, H.; Li, J.; Shao, H.; Jiang, T.; Liao, X.; Lu, S. One-Pot Preparation of Ni_2P/γ-Al_2O_3 Catalyst for Dehydrogenation of Propane to Propylene. *ChemistrySelect* **2018**, *3*, 10532−10536.
(43) Zhu, Q.; Zhang, H.; Zhang, S.; Wang, G.; Zhu, X.; Li, C. Dehydrogenation of Isobutane over a Ni−P/SiO_2 Catalyst: Effect of P Addition. *Ind. Eng. Chem. Res.* **2019**, *58*, 7834−7843.
(44) Xu, Y.; Wang, X.; Lv, R. Interaction between Cs and Ni2P/SiO2 for Enhancing Isobutane Dehydrogenation in the Presence of Hydrogen. *React. Kinet., Mech. Catal.* **2014**, *113*, 393−406.
(45) Kresse, G.; Furthmüller, J. Efficient Iterative Schemes for Ab Initio Total-Energy Calculations Using a Plane-Wave Basis Set. *Phys. Rev. B* **1996**, *54*, 11169−11186.
(46) Kresse, G.; Hafner, J. Ab Initio Molecular Dynamics for Liquid Metals. *Phys. Rev. B* **1993**, *47*, 558−561.
(47) Kresse, G.; Hafner, J. Norm-Conserving and Ultrasoft Pseudopotentials for First-Row and Transition Elements. *J. Phys.: Condens. Matter* **1994**, *6*, 8245−8257.
(48) Perdew, J. P.; Burke, K.; Ernzerhof, M. Generalized Gradient Approximation Made Simple. *Phys. Rev. Lett.* **1996**, *77*, 3865−3868.
(49) Taylor, A. Lattice Parameters of Binary Nickel-Cobalt Alloys. *J. Inst. Met.* **1950**, *77*, 585−594.
(50) Kibsgaard, J.; Tsai, C.; Chan, K.; Benck, J. D.; Nørskov, J. K.; Abild-Pedersen, F.; Jaramillo, T. F. Designing an Improved Transition Metal Phosphide Catalyst for Hydrogen Evolution Using Experimental and Theoretical Trends. *Energy Environ. Sci.* **2015**, *8*, 3022−3029.
(51) Monkhorst, H. J.; Pack, J. D. Special Points for Brillouin-Zone Integrations. *Phys. Rev. B* **1976**, *13*, 5188−5192.
(52) Henkelman, G.; Uberuaga, B. P.; Jónsson, H. A Climbing Image Nudged Elastic Band Method for Finding Saddle Points and Minimum Energy Paths. *J. Chem. Phys.* **2000**, *113*, 9901−9904.
(53) Hicks, J. C.; Jones, C. W. Controlling the Density of Amine Sites on Silica Surfaces Using Benzyl Spacers. *Langmuir* **2006**, *22*, 2676−2681.
(54) Zhao, D.; Feng, J.; Huo, Q.; Melosh, N.; Fredrickson, G. H.; Chmelka, B. F.; Stucky, G. D. Triblock Copolymer Syntheses of Mesoporous Silica with Periodic 50 to 300 Angstrom Pores. *Science* **1998**, *279*, 548−552.
(55) Rodriguez, J. A.; Kim, J.-Y.; Hanson, J. C.; Sawhill, S. J.; Bussell, M. E. Physical and Chemical Properties of MoP, Ni2P, and MoNiP Hydrodesulfurization Catalysts: Time-Resolved X-Ray Diffraction, Density Functional, and Hydrodesulfurization Activity Studies. *J. Phys. Chem. B* **2003**, *107*, 6276−6285.
(56) Monti, D. A. M.; Baiker, A. Temperature-Programmed Reduction. Parametric Sensitivity and Estimation of Kinetic Parameters. *J. Catal.* **1983**, *83*, 323−335.
(57) Lutterotti, L.; Bortolotti, M. Object Oriented Programming and Fast Computation Techniques in Maud, a Program for Powder Diffraction Analysis Written in Java. *IUCr Compcomm Newsl.* **2003**, *1*, 43−50.
(58) Ressler, T. WinXAS: A Program for X-Ray Absorption Spectroscopy Data Analysis under MS-Windows. *J. Synchrotron Radiat.* **1998**, *5*, 118−122.
(59) Rehr, J. J.; Booth, C. H.; Bridges, F.; Zabinsky, S. I. X-Ray-Absorption Fine Structure in Embedded Atoms. *Phys. Rev. B* **1994**, *49*, 12347−12350.
(60) Moula, M. G.; Suzuki, S.; Chun, W.-J.; Otani, S.; Oyama, S. T.; Asakura, K. The First Atomic-Scale Observation of a Ni2P(0001) Single Crystal Surface. *Chem. Lett.* **2006**, *35*, 90−91.
(61) Suzuki, S.; Moula, G. M.; Miyamoto, T.; Nakagawa, Y.; Kinosthita, K.; Asakura, K.; Oyama, S. T.; Otani, S. Scanning Tunneling Microscopy and Photoemission Electron Microscopy Studies on Single Crystal Ni2P Surfaces. *J. Nanosci. Nanotechnol.* **2009**, *9*, 195−201.
(62) Li, Q.; Hu, X. First-Principles Study of Ni_2P(0001) Surfaces. *Phys. Rev. B* **2006**, *74*, No. 035414.
(63) Ruban, A.; Hammer, B.; Stoltze, P.; Skriver, H. L.; Nørskov, J. K. Surface Electronic Structure and Reactivity of Transition and Noble Metals. *J. Mol. Catal. A: Chem.* **1997**, *115*, 421−429.
(64) Hammer, B.; Nørskov, J. K. Electronic Factors Determining the Reactivity of Metal Surfaces. *Surf. Sci.* **1995**, *343*, 211−220.
(65) Hook, A.; Celik, F. E. Predicting Selectivity for Ethane Dehydrogenation and Coke Formation Pathways over Model Pt−M Surface Alloys with Ab Initio and Scaling Methods. *J. Phys. Chem. C* **2017**, *121*, 17882−17892.
(66) Nykänen, L.; Honkala, K. Selectivity in Propene Dehydrogenation on Pt and Pt3Sn Surfaces from First Principles. *ACS Catal.* **2013**, *3*, 3026−3030.
(67) Becker, C.; Haubrich, J.; Wandelt, K.; Delbecq, F.; Loffreda, D.; Sautet, P. Adsorption of Simple Alkenes on Pt(111) and Pt−Sn Surface Alloys: Bond Strength versus Heat of Adsorption. *J. Phys. Chem. C* **2008**, *112*, 14693−14695.
(68) Xu, L.; Stangland, E. E.; Mavrikakis, M. Ethylene versus Ethane: A DFT-Based Selectivity Descriptor for Efficient Catalyst Screening. *J. Catal.* **2018**, *362*, 18−24.
(69) Persson, K. *Materials Data on Ni2P (SG:189) by Materials Project*; DOE Data Explorer: 2014.
(70) Oyama, S. T.; Wang, X.; Lee, Y.-K.; Bando, K.; Requejo, F. G. Effect of Phosphorus Content in Nickel Phosphide Catalysts Studied by XAFS and Other Techniques. *J. Catal.* **2002**, *210*, 207−217.
(71) Flaherty, D. W.; Hibbitts, D. D.; Gürbüz, E. I.; Iglesia, E. Theoretical and Kinetic Assessment of the Mechanism of Ethane Hydrogenolysis on Metal Surfaces Saturated with Chemisorbed Hydrogen. *J. Catal.* **2014**, *311*, 350−356.
(72) Morrow, B. A.; Sheppard, N. Infrared Spectra of Hydrocarbons Chemisorbed on Silica-Supported Metals. II. Ethylene on Nickel and Platinum over a Range of Temperatures. *Proc. R. Soc. London, Ser. A* **1969**, *311*, 391−413.
(73) Sheppard, N.; De La Cruz, C. Vibrational Spectra of Hydrocarbons Adsorbed on Metals: Part I. Introductory Principles, Ethylene, and the Higher Acyclic Alkenes. *Adv. Catal.* **1996**, *41*, 1−112.
(74) Castaño, P.; Elordi, G.; Olazar, M.; Aguayo, A. T.; Pawelec, B.; Bilbao, J. Insights into the Coke Deposited on HZSM-5, Hβ and HY Zeolites during the Cracking of Polyethylene. *Appl. Catal., B* **2011**, *104*, 91−100.
(75) Lange, J.-P.; Gutsze, A.; Allgeier, J.; Karge, H. G. Coke Formation through the Reaction of Ethene over Hydrogen Mordenite: III. IR and 13C-NMR Studies. *Appl. Catal.* **1988**, *45*, 345−356.
(76) Shen, J.; Hill, J. M.; Watwe, R. M.; Spiewak, B. E.; Dumesic, J. A. Microcalorimetric, Infrared Spectroscopic, and DFT Studies of Ethylene Adsorption on Pt/SiO_2 and Pt−Sn/SiO_2 Catalysts. *J. Phys. Chem. B* **1999**, *103*, 3923−3934.
(77) De La Cruz, C.; Sheppard, N. In Situ IR Spectroscopic Study of the Adsorption and Dehydrogenation of Ethene on a Platinum-on-

https://dx.doi.org/10.1021/acs.iecr.0c00908
Ind. Eng. Chem. Res. 2020, 59, 12666−12676

Silica Catalyst between 100 and 294 K. *J. Chem. Soc., Faraday Trans.* **1997**, *93*, 3569−3576.
(78) Zhao, Z.-J.; Chiu, C.; Gong, J. Molecular Understandings on the Activation of Light Hydrocarbons over Heterogeneous Catalysts. *Chem. Sci.* **2015**, *6*, 4403−4425.
(79) Arevalo, R. L.; Aspera, S. M.; Escaño, M. C. S.; Nakanishi, H.; Kasai, H. Tuning Methane Decomposition on Stepped Ni Surface: The Role of Subsurface Atoms in Catalyst Design. *Sci. Rep.* **2017**, *7*, 13963.
(80) Besenbacher, F.; Chorkendorff, I.; Clausen, B. S.; Hammer, B.; Molenbroek, A. M.; Nørskov, J. K.; Stensgaard, I. Design of a Surface Alloy Catalyst for Steam Reforming. *Science* **1998**, *279*, 1913−1915.
(81) Witzke, M. E.; Almithn, A.; Coonrod, C. L.; Hibbitts, D. D.; Flaherty, D. W. Mechanisms and Active Sites for C−O Bond Rupture within 2-Methyltetrahydrofuran over Ni, Ni12P5, and Ni2P Catalysts. *ACS Catal.* **2018**, *8*, 7141−7157.

https://dx.doi.org/10.1021/acs.iecr.0c00908
Ind. Eng. Chem. Res. 2020, 59, 12666−12676